**Ocean Science
Discussions**

Effect of variable winds on current structure and Reynolds stresses in a tidal flow: analysis of experimental data in the Eastern English Channel

K. A. Korotenko[1,2], A. V. Sentchev[1], and F. G. Schmitt[3]

[1]Laboratoire d'Océanologie et de Géosciences, UMR8187, CNRS, Université du Littoral Côte d'Opale, Wimereux, France
[2]P. P. Shirshov Institute of Oceanology, RAS, Moscow, Russia
[3]Laboratoire d'Océanologie et de Géosciences, UMR8187, CNRS, Wimereux, France

Correspondence to: K. A. Korotenko (kkorotenko@gmail.com)

| Discussion Paper | | Discussion Paper | | Discussion Paper | | Discussion Paper |

OSD

9, 2215–2254, 2012

Effect of variable winds on current structure and Reynolds stresses

K. A. Korotenko et al.

Title Page	
Abstract	Introduction
Conclusions	References
Tables	Figures

◄◄	►►
◄	►
Back	Close

Full Screen / Esc

Printer-friendly Version

Interactive Discussion

Abstract

Wind and wave effects on tidal current structure and turbulence throughout the water column are examined using an upward-looking acoustic Doppler current profiler (ADCP). The instrument has been deployed on the seafloor of 20-m depth, off the North-Eastern French coast in the Eastern English Channel over 12 tidal cycles and covered the period of the transition from mean spring to neap tide and forcing regimes varied from calm to moderate storm conditions. During storms, we observed gusty winds with magnitude reached $15\,\mathrm{m\,s^{-1}}$ and wave height reached up to 1.3 m. Analysis of velocity spectra revealed a noticeable contribution of wind-induced waves to spectral structure of velocity fluctuations within the upper 10-m layer. Near the surface, stormy winds and waves produced a significant intensification of velocity fluctuations, particularly when the sustained wind blew against the ebb tide flow. As during wavy periods the variance-derived Reynolds stress estimates might include a wave-induced contamination, we applied the Variance Fit method to obtain unbiased stresses and other turbulent quantities. Over calm periods, the turbulent quantities usually decreased with height above the seabed. The stresses were found to vary regularly with the predominantly semidiurnal tidal flow, with the along-shore stress being generally greater during the flood flow ($\sim 2.7\,\mathrm{Pa}$) than during the ebb flow ($\sim -0.6\,\mathrm{Pa}$). The turbulent kinetic energy production rate, P, and eddy viscosity, A_z, followed a nearly regular cycle with close to a quarter-diurnal period. As for the stresses, near the seabed, we found the maximum values of estimated quantities of P and A_z to be $0.1\,\mathrm{W\,m^{-3}}$ and $0.5\,\mathrm{m^2\,s^{-1}}$, respectively, during the flood flow. Over the storm periods, we found the highest stress values ($\sim -2\,\mathrm{Pa}$) during ebb when tidal currents were opposite to the southwesterly winds while, during the flood, the surface stresses slightly exceeded those estimated for a calm period.

1 Introduction

An understanding of turbulence and mechanisms of its generation in a tidal current are key goals of coastal physical oceanography, since turbulent processes are crucial in controlling flow dynamics and the vertical exchange of momentum and scalars within the water column. Knowledge of turbulence in shallow tidal channels is very important for making predictions about sediment and contaminant transports, vertical diffusion and bottom friction processes, as well as extremely important in modeling the mixing of oxygen, heat, nutrients and contaminants in the coastal ocean.

Hydrodynamic conditions at a shallow part of tidal channel as the Eastern English Channel (EEC) can vary from a relatively simple ebb-and-flood tidal system to a very complex one in which tide, wind stress, freshwater influx, and wind waves have significant forcing effects on the system (Brylinski et al., 1996; Sentchev and Korotenko, 2004, 2005; Sentchev and Yaremchuk, 2007; Korotenko and Sentchev, 2011). Wind and wave drift currents are variable and can be either reinforced or interfered with tidal currents, dependent on the phase of a tidal cycle. Particularly during stormy conditions, flow patterns may be highly complex.

The aim of this study is to investigate effects of wind and wave on tidal current, in particular their influence on spectral and turbulent structure of the current, looking at the vertical column turbulence through the relationships of the surface/bottom Reynolds stresses (hereafter RS), turbulent kinetic energy (TKE) production rate, P, and turbulent viscosity, A_z, estimated with the Variance Method (VM).

Since having been applied to oceanographic ADCP (an Acoustic Doppler Current Profiler) measurements by Lohrmann et al. (1990), the VM has been used successfully in a large number of studies of energetic tidal systems (Lu and Lueck, 1999a,b; Stacey et al., 1999; Rippeth et al., 2002, 2003; Fugate and Chant, 2005; Souza and Howarth, 2005; Nidzieko et al., 2006; Peters and Johns, 2006; Korotenko and Sentchev, 2011). However, in the presence of energetic surface gravity waves, the prediction of turbulent quantities with VM presents certain difficulties. The problem is that wind-induced waves

Effect of variable winds on current structure and Reynolds stresses

K. A. Korotenko et al.

Title Page

Abstract	Introduction
Conclusions	References
Tables	Figures

◀◀   ▶▶

◀   ▶

Back   Close

Full Screen / Esc

Printer-friendly Version

Interactive Discussion

can produce velocity variances of one order of magnitude larger than those associated with turbulence, and they often dominate the measured covariance between horizontal and vertical velocities. Since surface waves often occupy the same frequency range as marine turbulence, it is difficult to separate the latter from wave-induced velocity fluctuations using simple filtration. Therefore, development of various techniques and methods capable to remove the bias produced by surface waves from ADCP measurements of turbulent shear stress was an important issue over the past decade (Shaw and Trowbridge, 2001; Trowbridge and Elgar, 2003; Whipple et al., 2006; Feddersen and Williams, 2007; Rosman et al., 2008; Schmitt et al., 2009; Huang et al., 2010; Kirincich et al., 2010).

This paper addresses two challenges. Firstly, we perform a comprehensive study of velocity variations in the EEC, and spectral analyses of velocity fluctuations, during two typical periods (calm and storm conditions), and analyse the characteristic evolution of power density spectra in a wide frequency band. Secondly, we examine depth-time series of turbulent quantities in a tidal coastal flow, subject to wind forcing, in order to estimate its impact on turbulence variability throughout the water column in storm periods. In the paper, we present the ADCP observations of turbulence and its time-depth variability over twelve tidal cycles in a period of falling tide. Estimations of variance-derived RS, P and A_z were corrected using the Variance Fit (hereafter VF) method to remove the wave-induced contamination of these quantities. We also scrutinize and compare the turbulent quantities for storm and calm periods.

The paper is organized as follows: in Sect. 2, we describe the region of interest, experimental settings, measurements and data analysis. Velocity spectra are discussed in Sect. 3. In Sect. 4, we synthesize and examine the results obtained with the use of the variance method, and analyse the results for two periods with respect to forcing conditions. In Sect. 5, we summarize the obtained results. In Appendixes A and B, we shortly describe the variance and variance fit methods.

Effect of variable winds on current structure and Reynolds stresses

K. A. Korotenko et al.

Title Page

Abstract | Introduction

Conclusions | References

Tables | Figures

|◄ | ►|

◄ | ►

Back | Close

Full Screen / Esc

Printer-friendly Version

Interactive Discussion

1.1 Study area and ADCP deployment

Velocity measurements were performed in the Eastern English Channel (EEC), approximately 6 km offshore, northwest of the port of Boulogne-sur-Mer, France (Fig. 1). The area of interest is characterized by a tidal range of 7 m and current velocity amplitude close to $1.5\,\mathrm{m\,s^{-1}}$ at spring tide, and about $0.7\,\mathrm{m\,s^{-1}}$ during neap tide. Tidal currents have a predominantly semi-diurnal period with a pronounced fortnightly modulation due to interference of the major semi-diurnal constituents (M_2, S_2, N_2). A significant asymmetry of the sea surface elevation curve in the study area revealed the contribution of higher order non-linear harmonics (M_4, MS_4), which also generated a larger velocity during the flood flow as compared to ebb (Korotenko and Sentchev, 2011).

A 1.2-MHz upward-looking four-beam broadband RDI ADCP was deployed on the bottom (19 m mean water depth) for one-week period, from 9 to 16 June, 2009, covering tide evolution from spring to neap. The instrument was operated in fast pinging mode 12, providing one velocity profile per second. Each velocity record was an average of ten short pulse measurements over a second interval. Velocities were recorded in beam coordinates with 0.5 m vertical resolution (bin size), starting from 1.5 m above the bottom (midpoint of the first bin). The ADCP was mounted in a $\pm 20°$ gimbal to adjust for uneven bottom topography, although the instrument was slightly tilted (1.25°) with respect to the vertical. As was shown by Lu and Lueck (1999a), a 2° tilt results in no more than a 17 % bias in stress estimate for nonwavy conditions.

The orientation of the ADCP horizontal axes (heading) was chosen with respect to shoreline and dominant current direction (Fig. 1), so that the opposing beams 1 and 2, lying in the x-z plane, allowed us to estimate the cross-shore component of current velocity and Reynolds stress. Beams 3 and 4, lying in the y-z plane, on the other hand, allowed us to estimate the along-shore component of these quantities.

1.2   Forcing: wind and wave data

In subsequent analyses, we complemented velocity measurements by wind and wave data. Wind speed and direction were recorded at Boulogne-sur-Mer lighthouse (Fig. 1). Wave parameters (significant height, period, direction) were extracted from ADCP mea-
surements and CEFAS WaveNet archive (2009). The closest buoy to the experimental site was located off Dungeness (the south-eastern coast of England), about 30 km northwest from the ADCP site (Fig. 1). To account for possible spatial variations of principal wave parameters, we also used Wave Watch model (WW3) outputs in a grid point closest to the ADCP site (Fig. 1). The detailed description of the model configuration and parameterisation can be found in Rascle et al. (2008).

Figure 2 shows the wind record and time evolution of major wave parameters in response to wind forcing. Two different wind regimes could be identified during the experimental period. Winds blowing from southern and southwestern sectors, with moderate to strong speed (up to $10 \, \mathrm{m \, s^{-1}}$), were dominant during the period shown. Weaker winds ($\leq 6 \, \mathrm{m \, s^{-1}}$) from northern and northwestern sectors represented the second characteristic regime of the regional atmospheric circulation. Rapid changes in wind direction back and forth, occurring on a time scale of the order of a day, were a noticeable feature of the local wind variability. Calm and stormy weather conditions followed each other during the experiment. As seen, two calm periods were characterized by weak winds were from northern or southern sectors and low waves, which significant wave height, H_S, ranged from 0.3 to 0.6 m.

Figure 2 also reveals two distinct storm events which occurred during the observations. The first one began at 22:00 GMT on 10 June, lasted slightly more than one day, and peaked at the end of 11 June, when H_S reached 1.4 m. During 11 June, the southwesterly wind speed was close to $10 \, \mathrm{m \, s^{-1}}$, with gusts exceeding $15 \, \mathrm{m \, s^{-1}}$. These conditions caused an increase of the wave height from 0.3 to 1.4 m. For the early hours of 12 June, both wind speed and significant wave height dropped abruptly to $2 \, \mathrm{m \, s^{-1}}$ and 0.3 m, respectively. The evolution of the second storm event, on 15 June, followed

a similar scenario: growing speeds of southwesterly winds produced waves ascending from the west with wave height exceeding 1 m by the end of the day on 15 June (Fig. 2).

The comparison of H_S derived from ADCP pressure record and the SSH measured in Boulogne (Fig. 2b, c) revealed a complex modulation of waves by tide and wind variability. During both storm events when winds were mostly from the southwest, the significant wave height grew more rapidly on ebb than on flood. During those periods, waves propagated against the tidal current, that caused the increase of their steepness. For comparison, in Fig. 2c, we also show H_S measured by the Dungeness buoy and that predicted by the WW3 model. For storm periods, the growth of ADCP's H_S lagged that measured by the buoy while abrupt wave decay occurred similarly to the latter when winds ceased. Unlike H_S measured by the buoy and ADCP, that predicted by the WW3 model shows only a rough tendency of the wave growth/decay when wind increased/decreased, and reveal a longer period of wave decaying after the cease of stormy winds.

Understanding the combined effects of wave and wind forcing on the production of turbulence in the ocean is important for estimating shear-induced RS, as well as separating these forcings from other sources of turbulence. Such a source is the Langmuir circulation (LC), which significantly organizes the velocity structure in the wind-driven surface layer, during and after storm periods. LC appeared and developed at certain ratios between the wind stress and Stokes drift. The second calm period was especially interesting to us. According to Plueddemann et al. (1996), after storms, surface waves, which decayed more slowly than the wind, were apparently responsible for maintaining Langmuir circulation for long periods (up to 24 h) in the absence of significant wind forcing. In our case, as seen from after the first storm ($\sim$ 00:00 h on 11 June; Fig. 2) both winds and waves dropped abruptly and thus, during the following calm period conditions, for developing LC become unfavorable.

Stratification. The observational period was characterized by a homogeneous distribution of temperature and salinity throughout the water column. Only during calm periods, a weak diurnal thermal stratification appeared in the upper 2 m-layer principally

Effect of variable winds on current structure and Reynolds stresses

K. A. Korotenko et al.

Title Page

Abstract | Introduction

Conclusions | References

Tables | Figures

|◀ | ▶|

◀ | ▶

Back | Close

Full Screen / Esc

Printer-friendly Version

Interactive Discussion

Discussion Paper | Discussion Paper | Discussion Paper | Discussion Paper

on ebb or during current reversal. Stronger and steadier stratification (haline stratification) was typically observed in the EEC in winter and spring. It results from the fresh water input from a number of rivers on the Northeastern French coast and can affect nearshore water dynamics and transport (Sentchev and Korotenko, 2005; Korotenko and Sentchev, 2008; Sentchev and Yaremchuk, 2007). Saline stratification was not observed in the ADCP location because of a low supply of freshwater in June 2009.

2 Results and discussion

2.1 Time-depth variability of mean current and velocity shear

A general description of the evolution of SSH and currents off the northeastern coast of France is important for a better understanding of water dynamics and tidal-generated turbulence. Tidal currents in the EEC are rather strong with velocity amplitude up to $2\,\mathrm{m\,s^{-1}}$ observed in the Strait of Dover during the primary spring tide (Sentchev and Yaremchuk, 2007). When the current was northward (with a small eastward component) the sea surface first rose, then dropped. The period of rising tide lasted less then that of falling tide (Fig. 3b). When the current was southward, the duration of rising and falling tide period was also different (Fig. 3b). A lag between sea surface evolution and currents renders difficult the understanding of tidal motions in the region. The west-east velocity component accounts for shoreward displacement of water and causes the sea level to rise during the major part of the period (Fig. 3a). Therefore, this part of the tidal cycle period (positive cross-shore velocity component) is referred to as flood tide. The seaward (negative) cross-shore velocity component, which accounts for the level decrease for most of the time, marks the ebb tide. A peculiar feature of tidal dynamics in the EEC is the asymmetry of the SSH curve and current velocity with stronger currents occurring on flood, weaker on ebb, and high values of current acceleration observed during rising tide (Fig. 3b). Because of the strong asymmetry of the SSH curve, the period of falling tide exceeds that of rising tide by approximately 2 h. Moreover, the

tidal current lags the sea level by approximately 2.5 h. Therefore, the surface current reversal (S-N component) occurred 2.5 h and 3 h before the arriving of the high water or low water, respectively, in Boulogne. A counter-clockwise veering of current vector with depth could be also recognised in the point of the ADCP location. Note that ebb and flood periods could be easily defined using zero velocity contours in the field of the cross-shore velocity component shown in Fig. 3a.

The modeling study by Sentchev and Korotenko (2005) showed that, in the region of interest, the tidal transport was larger on the flood than on the ebb, so that there was a net residual transport to the northeast. Detailed examination of local hydrodynamics revealed that there was a rectification of the tidal flow by non-linear effects (enhanced by fresh water inflow) that produced a net residual northward flow along the French coast. The residual velocity ranged from $0.15\,\mathrm{m\,s^{-1}}$ at neap tide, to $0.25\,\mathrm{m\,s^{-1}}$ at spring tide.

As shown in Fig. 3, during the present experiment conducted in the period of a tide transition from spring to neap, the mean current velocity reached maximal magnitudes at the surface while the majority of the velocity shear was near the seabed. Figure 3 also revealed that along- and cross-shore components of velocities and their shears were tidally forced and exhibited semidiurnal variability. The along-shore velocity exceeded $1.1\,\mathrm{m\,s^{-1}}$ on the flood flow and $-0.7\,\mathrm{m\,s^{-1}}$ on the ebb flow, while the across-shore velocity component was much weaker and its magnitude did not exceed $0.4\,\mathrm{m\,s^{-1}}$. Note that storm periods could distinctly be recognized due to "knotted" lines of zero-mean shear of both components of current velocity (Fig. 3c, d). Velocity shears, during both storms, significantly decreased near the sea surface, and they were gradually beginning to restore when winds ceased. This can be clearly seen from the sum of the velocity components shear squared,

$$S_{uv}^2 = \left[\left(\frac{\partial \overline{u}}{\partial z} \right)^2 + \left(\frac{\partial \overline{v}}{\partial z} \right)^2 \right]$$

for three-day period following the first storm (Fig. 3e). During the latter, the zero magnitude of S_{uv}^2 appeared at the sea surface (the same for the second storm event), while during the calm period following the storm, minimum magnitudes of S_{uv}^2 were found only along vertical lines specifying time and position of the water slack, where current velocities and shears were weak. Hereafter we conventionally refer to the water slack as a moment when a flow passes through a minimum.

2.2 Velocity spectra

For the analysis of velocity spectra, we used power spectral density obtained with a complex Fast Fourier Transform (FFT) with a Nyquist frequency of 0.5 cycles per second (cps). The essential requirement for applying a classical FFT method is the continuity of the data record. Therefore, the time series of the current velocity components were inspected for gaps in the initial 1 cps sampled data. Their analysis revealed that, in the layer ≤ 12 m above the bottom (mab), the data had no gap longer than 6 s, while all gaps discovered shorter than 6 s, were linearly interpolated. The data in the upper layer (> 12 mab) were excluded from subsequent spectral analysis.

Figure 4 shows the power spectral density of cross-shore, u, and along-shore, v, components, of the velocity vector at 2 and 10 mab, recorded during the second calm period. Spectra of both components had a maximum at the semidiurnal cyclic frequency 0.08 cycles per hour (cph), while the diurnal, which peaked at 0.04 cph was not clearly pronounced because of a short fft-length. As Korotenko and Sentchev (2011) showed, in the EEC, the diurnal peak was of the same order of magnitude as the quarter-diurnal peak at $f \approx 0.16$ cph (f denotes frequency). At frequencies higher than 6 cph, spectral slopes varied between -1 and -5. Figure 4 also indicates that in deeper layers, where the influence of wind waves were insignificant at frequencies $f > 300$ cph, the spectra were reminiscent of the inertial subrange with spectral slopes close to $-5/3$ (Fig. 4b). However, most slopes in the spectra presented departures from $-5/3$ (see discussion below).

Title Page

Abstract | Introduction

Conclusions | References

Tables | Figures

◄ | ►

◄ | ►

Back | Close

Full Screen / Esc

Printer-friendly Version

Interactive Discussion

Analysis of spectra at 2 and 10 mab revealed that current velocity variations, at frequencies less than 0.5 cph, followed almost the same trend throughout the water column, indicating barotropic behavior of the flow field. At frequencies > 0.5 cph, the spectra showed that the oscillations were intensified near the seafloor and expanded up to the middepth, indicating an energetic type of motion, controlled by the bottom boundary layer. Along-shore and cross-shore current spectra showed a different amount of energy at frequencies < 60 cph throughout the water column, while at higher frequencies (> 60 cph), the amount of energy was roughly the same. Figure 4 also shows that, in the frequency range 0.08–0.3 cph, the power spectral density of both velocity components are reminiscent of a "red"-type spectrum, but was interrupted by the peak of energy at 0.5 cph, and a shoulder ranged between 0.8 and 10 cph. At frequencies 0.3–0.4 cph, the variance-preserving form of the spectra (not shown here) revealed a distinct energy gap lying between a low-frequency (barotropic) oscillations and a high-frequency turbulence interval.

Figure 4a shows the energy spectrum peaked at 300–600 cph and represented by a bimodal structure that corresponded to waves with periods of about 5 and 10 s. These wave periods have been also revealed from the data recorded by the CEFAS buoy. The longer wave period appeared to be associated with swell, because its energy decreased much slower with depth, as compared with wind-induced wave energy that fell abruptly with depth. Note that, near the seabed during our observations, either swells or wind waves, made a relatively small contribution to the power spectra.

2.3 Comparison of spectra for storm and calm periods

Before analyzing and comparing velocity spectra for the storm and calm periods, we examined the structure of current velocity obtained with the ADCP. For the purpose of this paper, herein we limited our attention to the first storm period and its following calm period, as shown in Fig. 2b. Following Lu and Lueck (1999a), we analyzed a one-day-long time series of the along-shore velocity at middepth, estimated from beam 3 and 4 data with one second resolution. The low- and high-frequency variations were

Title Page

Abstract Introduction

Conclusions References

Tables Figures

◄◄ ►►

◄ ►

Back Close

Full Screen / Esc

Printer-friendly Version

Interactive Discussion

separated by applying a zero-phase, low-pass and fourth-order Butterworth filter with a cut-off period of 20 min.

Figure 5 illustrates the comparison of the along-shore velocity constituent for the storm and calm periods. The upper curve is the raw data of six-ping averages collected every 1 s. The middle curve is the same data with 20-min smoothing and offset by 1.0 m s^{-1}. The lower curve is the alongshore velocity fluctuation formed by taking the difference of the upper two curves and offset them by 2.5 m s^{-1}.

For both periods, the raw velocity time series exhibited a wide range of time scales from high-frequency turbulent fluctuations to slow variations on time scales of the order of the record lengths. As Fig. 5 shows, high-frequency velocity fluctuations varied in agreement with the low-frequency flow with a velocity minimum during the slack water periods. For the storm period, the raw and residue data indicated intensive velocity fluctuations associated with surface gravity waves that can be clearly seen in the spectra presented below.

Figure 6 represents power spectral density of near bottom horizontal velocity components, estimated for the 25-h storm and calm periods shown in Fig. 5. To focus on the turbulent part of the spectra, they were plotted within the frequency range > 0.00167 cps (∼ 6 cph) and presented in cps-scale for clarity. Note that the frequency range well above 6 cph was similar to the inertial subrange of three-dimensional turbulence, even though its spectral slope was not exactly −5/3.

A comparison of spectra for both periods indicated characteristic discrepancies in the distribution of spectral energy, particularly associated with level of spectral energy. That is, frequencies 0.00167–0.01 cps, larger for along-shore velocity that for cross-shore one. In addition, the spectra for the storm period, were characterized by a sharp wave peak centered at ∼ 0.2 cps (2 s) and further above 0.2 cps a spectral slope is close to −5 while, for the calm period, the spectra contained a broad but poorly pronounced peak centered at ∼ 0.1 cps (10 s). Further above 0.2 cps, a spectral slope was close to −5/3. As seen, the wave energy, which penetrated in the near bottom layer was lower

Effect of variable winds on current structure and Reynolds stresses

K. A. Korotenko et al.

Title Page

Abstract	Introduction
Conclusions	References
Tables	Figures

|◄ | ►|

◄ | ►

Back | Close

Full Screen / Esc

Printer-friendly Version

Interactive Discussion

than the energy of the underlying stress-carrying eddies which filled the range between 0.00167 and 0.05 cps (i.e., between 1 min 30 s and 10 min).

Departure from the slope of −5/3, at first glance, could have indicated that there was no exact local isotropy (see Tennekes and Lumley, 1972) in the turbulent flow we observed. Although, in our case, the departure may have also been associated with the impact of wind waves, of which significant heights reached 1.3 m during storm periods. The impact would have been particularly pronounced near the sea surface and thus, measuring velocities under storm conditions, the slope of the inertial subrange spectra would have been more affected by wave motion near the sea surface than in bottom layers, where one might have expected a well pronounced the inertial subrange spectra $f^{-5/3}$. During nonwavy conditions, the inertial subrange should have been pronounced in spectra throughout the water column. However, our results have shown that departures of the slope from −5/3, in the inertial subrange, were found for all computed velocity spectra and weakly depended on weather condition and depth. Such peculiarity of spectra within the turbulence interval is likely to be associated with a method used for processing velocity measurements obtained by ADCPs. Comparing velocity spectra computed for velocities measured by ADV and ADCP in the range 0.01–1 cps, Nidzieko et al. (2006) showed that ADV spectra always exhibited spectral decay, which closely followed the −5/3 slope. By contrast, the inertial subrange of three-dimensional turbulence was not readily seen in the ADCP spectra; within the same frequency range, the slope of ADCP (mode-12) spectra was close to −1. Peters et al. (2007) demonstrated that reducing ADCP instrumental noise could improve spectral shape in the inertial subrange.

To provide more details in the response of currents to wind and wave forcing we have shown in Fig. 7 depth-frequency spectra of the along-shore velocity computed for the first storm and calm period on 13 June. In order to adjust a color palette and emphasize the wave peak, the spectra were presented for frequencies $f > 0.4$ cph. As seen, features of the spectra, for both periods, had a tendency to line up parallel to the depth-axis and the major energy-containing band extended roughly up to $f \approx 5$ cph covering

the entire water column. At the same time, Fig. 7 reveals significant differences in spectral energy distribution. The storm period was characterized by an amplification of energy throughout the water column with some gaps of energy at different depths. One of them, already mentioned above, was at 5 mab between 0.4 and 0.5 cph. The calm period following the storm was characterized by a general attenuation of energy in the range from 0.4 to 20 cph, and some harmonics were significantly suppressed during a relaxation period after the storm. High-frequency margins of the energy-containing band, covering the range from ∼ 5 to 11 cph for both periods, showed that the spectral energy intensified toward the seabed, which is a characteristic of wall-bounded turbulence. It is also remarkable that structures of the spectra, in the interval 40–110 cph, practically did not change, regardless of the intensity of wind and/or wave forcing.

Figure 7 also demonstrates distinct differences at highest frequencies for the storm and calm periods. During the storm, the spectrum, presented in Fig. 7a, indicated an energetic spectral peak associated with velocity fluctuation caused by wind action (wind waves, their breaking and instability of drift current). This peak centred at 450 cph and covered the entire water column. During the calm period, spectrum in Fig. 7b shows a weak wave peak at lower frequencies corresponding to velocity fluctuations generated by swells.

2.4   Reynolds stress and mean velocity shear

Current measurements revealed a complex structure of tidal flow in the shallow coastal zone, particularly when tidal forcing was accompanied by the action of variable winds and waves. To elucidate the combined effect of tides, winds and waves on turbulence variability in the water column, we begin from analyses of the structure and evolution of the Reynolds stress for the first calm and storm periods, as they indicated in Fig. 2. Following Rippeth et al. (2002), we show in Fig. 8 vertical profiles of hourly-averaged Reynolds stress, τ_y (row a), acting in the along-shore direction for each hour during one tidal cycle. To give a complete impression of the mean velocity, stress and shear variations over a semidiurnal cycle, together with the profiles of Reynolds stress, we

show the along-shore components of the mean current (row b) and velocity shear, S_V (row c). All profiles were hourly averaged within a tidal cycle. For the shear (Fig. 8c), tic marks given along the horizontal axis correspond to a zero crossing of the profile in question. For an individual shear profile, the scale ranges from $-0.07 \, \mathrm{m \, s^{-1}}$ to

5 $0.07 \, \mathrm{m \, s^{-1}}$ as indicated in Fig. 8c. The velocity profiles showed that, for both ebb and flood flows, the largest velocities were observed near the sea surface. Near the bottom, velocities had a logarithmic profile.

The calm period. During the calm period, shear and most of the stresses, shown in Fig. 8 (left panel), have a tendency to decrease more or less regularly from extreme

10 values near the seabed to lower values at the highest level observed ($\sim 5 \, \mathrm{m}$ below the surface). However, some stress profiles greatly depart from this tendency indicating that besides the bottom-shear production, other mechanisms appeared to contribute to the Reynolds stresses in upper layers (cf. Rippeth et al., 2002).

Near the sea surface, despite the moderate forcing, a noticeable influence of wind

15 and waves was clearly seen. Around slack water, the stresses and shears throughout the water column should be close to zero. However, as Fig. 8a showed us, stress profiles corresponding to the reversal flow revealed more complicated, "curling back" structures, (e.g. profile 1 of τ_y in Fig. 8a) which were certainly associated with surface forcing, and played a significant role during the weak flow period. The largest

20 stress magnitudes and shear occurred at times of highest flow speeds. The stresses indicated a considerable asymmetry between the ebb and flood. During the flood, near-bed stress and shear exceeded $2.7 \, \mathrm{Pa}$ and $0.08 \, \mathrm{s^{-1}}$, respectively, at the time of maximum depth mean flow speed ($\sim 1.1 \, \mathrm{m \, s^{-1}}$) while during the ebb the stresses and shear were limited to $\sim -0.8 \, \mathrm{Pa}$ and $-0.07 \, \mathrm{s^{-1}}$ during the peak ebb, depth-mean, flow

25 of $\sim -0.7 \, \mathrm{m \, s^{-1}}$.

The storm period. As was mention above, for the study area, sustained winds blowing from southwest produced waves that propagated in the direction opposed to the ebb flow. Such waves, due to a tendency to steepen, were able to break over the ebb shoal, dissipating energy in a sub-surface layer and homogenizing the latter. As was shown

by Terray et al. (1996), the homogeneous sub-surface layer extends to $Z_b = 0.26K_p^{-1}$, where K_p is the peak wavenumber of the local wind sea. In contrast, during flood tide, sea surface waves propagating with the currents were elongated and hence, conditions for wave breaking became less favourable. Thus, during storm periods, particularly when the wind blows against the ebbing tide, we observed a significant enhancement of turbulence while, during the flood tide, turbulence generation near the sea surface was moderate. Earlier, a similar effect has been reported by Seim (2002) and Rippeth et al. (2003).

Next, to illustrate the significance of wind and wave effects on the Reynolds stress, we present in Fig. 8a (right columns) the uncorrected along-channel stress. Below, we apply a method to eliminate wave-induced bias from the stress estimates. As seen, the comparison of the intensity of time-depth variations of the Reynolds stresses acting during calm periods revealed significant differences with those acting during the storm periods (cf. left and right columns of Fig. 8a). The main difference was that magnitudes of the Reynolds stress, during the storm period, were much larger throughout the column than those estimated for the calm period. On the flood flow, above ~ 7 mab, profiles of the "storm" stress indicated a distinct reversal tendency remaining positive. During the ebb, stress magnitudes, remaining negative, approached −2.8 Pa at 12 mab revealing a strong combined effect of the wave-induced bias and shear-induced turbulence produced by storm in the sea surface layer.

2.5 Time-depth variation of turbulent quantities

Figure 9 shows the depth-time sections of the 20-min mean estimates of turbulent quantities computed by applying the variance method (see Eqs. A1–A3 in Appendix A) from which the wave-induced contamination were removed by a use of the variance fit method (Appendix B). The presented results cover the entire period of measurements. It is obvious that computed stresses and inferred turbulent quantities are somewhat noisy and the right way to present them is to show composite patterns formed by

Effect of variable winds on current structure and Reynolds stresses

K. A. Korotenko et al.

Title Page

Abstract	Introduction
Conclusions	References
Tables	Figures

| ◄ | ► |
| ◄ | ► |

| Back | Close |

Full Screen / Esc

Printer-friendly Version

Interactive Discussion

averaging, for example, 4 tidal cycles as have been done by Peters (1997) and Rippeth et al. (2002). In our case, unfortunately, weather conditions were changing so rapidly such that composite plots would not have been representative. Therefore, we have presented our results as they were.

5   *Reynolds stresses.* Plotted in the panels a and b of Fig. 9, wave-unbiased cross- and along-shore components of RS, show regular variation over 12 tidal cycles. During the flood, both stresses were positive (warm shading) and generally decreased with increasing height. During the ebb, both stress components were negative (cool shading) and their magnitudes, in the lower half of the water column, also decreased with
10   increasing height above the bottom. Above middepth, the along-shore stress frequently reversed its sign, corresponding to the sign reversals of the along-shore shear; a good evidence of that were oblique contour lines during the period of current reversal. Similarly, to the along-shore stresses, the cross-shore stresses were smaller during the ebb flow than those during the flood. The extremely large stresses obtained near the sea
15   surface during the tidal current reversal are certain to be associated with the wind and wave influences. As discussed above, large stresses appeared during the entire period of the storms, and they were significantly enhanced by southwesterly winds in cases when they blew during the ebb tide. Figure 9a, b illustrate this phenomenon during the storm on 11 June 2009. As seen, near surface stresses were large during entire storm
20   period, but became extremely large during the ebb tide.

Figure 9 also reveals a pronounced asymmetry of stress magnitudes between the ebb and flood. In calm periods, the stress cycle was seen to be highly regular and dominated by the along-shore component that exceeds 2 Pa, while the cross-channel stress τ_y rarely exceeded a magnitude of 0.7 Pa. Another aspect of asymmetry of the
25   stresses was evident in their behavior during successive water slacks. Around low water slack, the period of low stress (< 0.5 Pa) lasted ~ 2 h compared to ~ 1 h around high water slack.

The near bottom RS and the mean tidal currents were highly correlated and near the seafloor, the stress exhibited a quadratic drag law behavior. Drag coefficient, C_D

strongly depended on the phase of the tide. Its estimates, based on the 10 min averaged full set of data, varied systematically between 0.0012 on ebb and 0.0022 during flood (Fig. 10).

TKE production rate. Shown in Fig. 9c, the TKE production rate, P, was estimated from the product of the Reynolds stress and the velocity shear according to Eq. (A2). It indicates the amount of energy that is transferred from the mean flow to turbulent kinetic energy. In a tidal flow for nonwavy conditions, P intensified toward the seabed, which is a characteristic of wall-bounded turbulence. The magnitude of P spanned about four decades, ranging from about $10^{-1}\,\mathrm{W\,m^{-3}}$ near the bottom to $\sim 10^{-5}\,\mathrm{W\,m^{-3}}$ during weak flows. Note that either negative values of P appeared due to round-off, or they were caused by unreliable stress estimates obtained during the turning of the tide. We therefore removed negative estimates of P, substituting them by the limit value of $10^{-5}\,\mathrm{W\,m^{-3}}$. The rate of TKE production was related to the magnitude of the current velocity and exhibited a dominant quarter-diurnal variation throughout the water column, with the exception of the uppermost layers, where strong wind and wave forcing can interact with the diurnal current muting M4 response. As with the stress, there was a clear asymmetry in P between flood and ebb; for our deployment, the near seabed peak ebb value of P was typically an order magnitude less than that observed at maximum flood.

Turbulent viscosity. The eddy viscosity coefficient A_z, presented in Fig. 9c, was calculated by dividing P by the shear squared according to Eq. (A3). The variations of A_z ranged from about $10^{-5}\,\mathrm{m^2\,s^{-1}}$ during weak flows to $0.3\,\mathrm{m^2\,s^{-1}}$ during strong flows. Generally, the eddy viscosity increased with increasing height above the bottom in the lower half of the water column, and reached a maximum near the middepth during calm periods. During the storm, the maximum of A_z moved upward and reached about $0.5\,\mathrm{m^2\,s^{-1}}$ at 12 mab.

3   Conclusions

We measured turbulence in the shallow zone of the Eastern English Channel with a bottom-mounted, upward-looking, four-beam, 1.2-MHz ADCP RDI "Workhorse". The measurements covered over 12 tidal cycles for the period of the transition from mean spring to neap tide. During the observations, we identified different forcing regimes based on the wind stress and wave height records.

To our knowledge, the presented investigation of turbulence quantities and their evolution under tidal and unstable wind forcing, is the first one conducted in a particular region of the EEC, which, as revealed, was characterized by a specific asymmetry of tidal cycle that echoes the evolution of turbulent quantities. We limited this work to the presentation of the ADCP data, and straightforward processing of these data such as spectra and variance derived RS, TKE production rate and turbulent viscosity. To use the variance method for the unbiased stresses estimates, we applied the VF method, which allowed removing the majority of the wave-induced contamination of RS.

The following summarizes our results and demonstrates effects of variable forcing regimes on turbulent quantities in tidal flow. During the observation period, weather changed from calm to moderate storm events with gusting winds reached $\sim 15\,\mathrm{m\,s^{-1}}$ and significant waves height of about $1.5\,\mathrm{m}$. During calm periods, wind speed and significant height did not exceed $5\,\mathrm{m\,s^{-1}}$ and $0.5\,\mathrm{m}$, respectively.

The recorded velocities exhibited both strong variations at tidal frequencies and high-frequency fluctuations During the calm periods, the RMS velocity was found to be of the order of a few $\mathrm{cm\,s^{-1}}$, and about few tens of $\mathrm{cm\,s^{-1}}$ during storm events. Shears were maximal ($\sim 0.08\,\mathrm{s^{-1}}$) near the bed, and decreased with height above the bottom. Above 5 mab, the shear on the ebb flow extended to the surface during low wind forcing and was close to zero on the flood flow, but could be of either sign in the upper water column when the winds exceeded $5\,\mathrm{m\,s^{-1}}$. Southwesterly winds reinforced the flood tide shear, and decreased it in the upper water column during the ebb. It is remarkable that, during the strong wind and wave forcing, zero-mean magnitudes of shear squared

Effect of variable winds on current structure and Reynolds stresses

K. A. Korotenko et al.

|◄ | ►|

◄ | ►

Back | Close

Full Screen / Esc

Printer-friendly Version

Interactive Discussion

S_{uv}^2 appeared near the sea surface, indicating strong mixing, while during calm periods, such magnitudes were visible along vertical lines, specifying the locations of slack waters.

In this paper, we paid much attention to analysis of the velocity spectra for both calm and storm periods. Generally, within the range between 0.08 cph (semidiurnal tide) and 0.3 cph, velocity spectra were reminiscent of red-type spectra that were interrupted by a shoulder at 0.6–10 cph. In the variance-preserving form, spectra revealed a distinct energy gap at frequencies 0.3–0.4 cph lying between low-frequency barotropic and high-frequency harmonics. At frequencies > 0.3 cph, the spectra indicated several fully resolved maxima at energy-containing ranges, and a bimodal peak at the highest frequencies associated with contributions of surface waves. Within the spectral range from 0.6 cph to 100 cph, the spectral slope was close to –1 while at the highest frequencies ($f \geq 500$) the spectral slope, in the presence of waves, was close to –5. Most of the spectra departed from the $f^{-5/3}$ regime, except at frequencies $f \geq 300$ cph. For this frequency band, the spectra usually corresponded to the inertial subrange in the absence of surface waves. During the storm and calm periods, the spectral energy intensified toward the seabed within the band 5–11 cph, which is characteristic of wall-bounded turbulence. In the interval 40–110 cph, the structure of the spectra almost did not change, regardless of wind and wave forcing.

The variance-derived turbulent Reynolds stress was resolved from 1.5 m to 12 m height (mean depth was 20 m). Most of the time, the stress was aligned with the current throughout the water column, except for slack periods when mean current and stress vectors greatly departed from each other. Stress magnitudes ranged from a detection threshold of ∼ 0.05 Pa to a maximum of ∼ 2.6 Pa. For calm periods, we found that the Reynolds stress decreased more or less regularly from high values near the bottom by 70 %–80 % toward the top of the ADCP range. For the storm periods, the stress first decreased from high values near the bottom toward middepth, and then increased again up to 2.8 Pa under the influence of wind and surface waves. The examination of the Reynolds stresses and shear profiles revealed that the near surface

stress was highest during southwesterly winds, and peaked during the ebb. In these conditions, tidal current opposed wind wave propagation that caused wave breaking due to a mechanism of wave shoaling. Therefore the near-surface maxima in the RS associated with southwesterly winds raised the intriguing possibility of measuring the momentum flux associated with wave breaking.

The rate of TKE production ranged from $\sim 10^{-1}\,\mathrm{W\,m^{-3}}$ near the bottom to a detection threshold of $\sim 10^{-5}\,\mathrm{W\,m^{-3}}$ during watter slack periods. The bottom-generated turbulence extended to the near surface during the flood but was typically located within the layer 1.5–8 mab during the ebb. However, during periods of strong southwesterly winds, and breaking waves over the ebb shoal, we found that the TKE production rate increased near the sea surface. Generated near the surface and propagating downward, this turbulence merged the shear induced bottom turbulence propagating upward. For that reason, for periods of strong southwesterly winds, we observed high magnitudes of Reynolds stresses and TKE production rates throughout the water column. Estimation of the drag coefficient revealed strong dependency on the phase of tide. Its value varied between 0.0012 on ebb and 0.0022 during flood.

Finally, it is worth noting that the combination of ADCP measurements and wind/waves observations offers significant advantages for performing analysis of ADCP data, and allows interpreting the obtained results more correctly. Besides the study of turbulent quantities in the bottom boundary layer we were particularly interested in comparing those computed for calm and storm events, since their time-depth variability reflected an unique interaction between winds, waves and tidal currents. We found that, for the storm periods, variance derived and wave-unbiased turbulent quantities significantly increased on ebb flow in cases when winds were from the southwesterly sector. In that event, tidal currents opposed wave propagation and enhanced wave breaking due to the mechanism of wave shoaling. By contrast, on the flood, sea surface waves propagating with the currents were elongated, and hence, turbulence production due to the wave breaking mechanism appears to be less likely than during the ebb. During

calm periods, turbulent quantities indicated their growth toward the seabed, which is a characteristic of wall-bounded turbulence.

Obtained vatiance-derived turbulent quantities uncontaminated by the waves, further, we suppose to use for tuning numerical models earlier exploited in the EEC (Korotenko and Sentchev, 2004, 2008; Sentchev and Korotenko, 2004, 2005, 2007).

Appendix A

Variance method

For the upward looking ADCP in a Janus configuration (Lu and Lueck, 1999b), a relationship between the velocity along the four beams, V_i (positive toward the instrument) to those in Cartesian coordinates u, v and w allows inferring RS:

$$\frac{\tau_x}{\rho} = -\overline{u'w'} = \frac{\left(\overline{V_2'^2} - \overline{V_1'^2}\right)}{2\sin 2\theta}, \qquad \frac{\tau_y}{\rho} = -\overline{v'w'} = \frac{\left(\overline{V_4'^2} - \overline{V_3'^2}\right)}{2\sin 2\theta} \qquad (A1)$$

Here $i = 1$–4 represents the ADCP beam number, u', v' and w' are turbulent fluctuation components of velocity obtained after the decomposition of the raw velocity (u, v, w) into a mean velocity $(\overline{u}, \overline{v}, \overline{w})$ and a turbulent part (u', v', w'), θ is the half angle between opposing beams (20° for the ADCP we used), and ρ is water density. The overbar denotes a time-averaged velocity at chosen interval (20 min). Note that to derive the mean velocity vector, we needed to assume that the mean flow was statistically homogeneous in the horizontal space over distances separating the beams, that is, $\overline{u}_1 = \overline{u}_2$. To derive the Reynolds stress, it had to be assumed that all the second-order moments of turbulent velocity fluctuations were horizontally homogeneous, that is, $\overline{u_1'^2} = \overline{u_2'^2}$, $\overline{u_1'w_1'} = \overline{u_2'w_2'}$, etc.

In Eq. (A1), we omitted the terms describing noise errors due to pitch and roll of an ADCP. As was shown by Lu and Lueck (1999b), and Peters and Johns (2006),
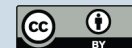
the contribution of such terms could be neglected even for relatively significant roll and pitch angles in the absence of surface gravity waves. However, in the presence of energetic surface waves, wave bias can contaminate or even dominate Reynolds stress measurements, even for a small tilt in sensor alignment. This effect will be discussed and assessed in Appendix B.

Estimations of TKE production rate. The rate at which energy was transferred from the mean flow to the turbulent kinetic energy through the interaction of the turbulence with the shear was estimated from the scalar product (between matrices, often called double dot product) of the Reynolds stress and the mean velocity shear:

$$P = -\rho \left[\overline{u'w'}\frac{\partial \overline{u}}{\partial z} + \overline{v'w'}\frac{\partial \overline{v}}{\partial z} \right] \tag{A2}$$

where both the stress and velocity shear were estimated from the ADCP data. Because of the alignment of the ADCP to the tidal flow, being itself globally oriented in S-N direction, we would have expected the main contribution to the rate of production to come from the second term on the right-hand side of Eq. (A2).

The estimate of the vertical viscosity coefficient, A_z was calculated by the TKE production rate, P, dividing with a sum of mean velocity shear squared components. This yielded

$$A_z = \frac{1}{\rho}P \left[\left(\frac{\partial \overline{u}}{\partial z}\right)^2 + \left(\frac{\partial \overline{v}}{\partial z}\right)^2 \right]^{-1}. \tag{A3}$$

Results from Eqs. (A1)–(A3) were sensitive to the averaging time interval chosen in the Reynolds decomposition. As was mentioned above, we used an averaging interval of 20 min, a choice justified by the examination of Reynolds stress spectra by Lu and Lueck (1999b) who revealed that comparatively low frequencies could also contribute to the stress. Technically, the high- and low-frequency velocity components were separated by fourth-order Butterworth filter at zero phase. Variances of beam velocity

Title Page

Abstract | Introduction

Conclusions | References

Tables | Figures

◄ | ►

◄ | ►

Back | Close

Full Screen / Esc

Printer-friendly Version

Interactive Discussion

fluctuations were then calculated and smoothed with the same filter and averaged over 20 min intervals to give estimates of the Reynolds stress.

Not that despite the efficiency of the VM in assessing turbulent quantities this method, however, can be broken down in the presence of even modest surface gravity waves, as they produce large along beam variances that become dominant near the sea surface Rippeth et al. (2003). Therefore, removing the wave-induced bias in RS is an important task of ADCP data pre-processing. As we noted above, there are a number of methods developed for decontamination wave-induced bias of RS. In our work, for this, we have chosen the VF method described below.

Appendix B

Variance fit method

Bias introduced by waves. In the presence of waves, the instantaneous velocity can be decomposed into a mean (e.g., $\overline{v}$) associated with the slowly varying flow, a component associated with the waves (e.g., $\tilde{v}$), and a fluctuation associated with the turbulence (e.g., v'), so that

$$v = \overline{v} + \tilde{v} + v'$$
$$w = \overline{w} + \tilde{w} + w' \tag{B1}$$

Assuming that the wave and turbulence components of the signal are uncorrelated, direct application of VM to Eq. (B1) for beams 3 and 4 according to Rosman et al. (2008) gives

$$\frac{\overline{(\tilde{u}_4 + v'_4)^2} - \overline{(\tilde{u}_3 + u'_3)^2}}{4 \sin\theta \cos\theta} = E_{\text{ws}} + E_{\text{tilt}} + E_{\text{turb}} \tag{B2}$$

Title Page

Abstract | Introduction

Conclusions | References

Tables | Figures

◀ | ▶

◀ | ▶

Back | Close

Full Screen / Esc

Printer-friendly Version

Interactive Discussion

Eq. (B2) shows that the errors due to wave bias can be categorized as (1) E_{ws}, the real wave stress $-\overline{\tilde{u}\tilde{w}}$, or (2) E_{tilt}, the error due to the interaction of wave orbital velocities and instrument tilt $\sim \left(\overline{\tilde{u}^2} - \overline{\tilde{w}^2} \right)$.

Wave bias correction. To assess the wave bias in RS, Whipple et al. (2006) proposed VF method, which later was tested by Rosman et al. (2008) for different datasets. Based on Trowbridge's (1998) approach and extended to ADCPs by Whipple et al. (2006), this method assumes that wave orbital velocities are in phase along any one ADCP beam and decay with depth according to linear wave theory. The decay of wave velocity between bins chosen for differencing is determined from a fit to the vertical profile of the variance of beam velocity.

Following Whipple et al. (2006), we subtracted velocities in bins that were separated by distances greater than the correlation distance of the turbulence ($\sim$ 1–2 m). In this case, we reduced the impact of waves on RS and minimized the amount of turbulent energy that was removed by the subtraction of velocity along each beam. The horizontal component of the separation was chosen to be small with respect to the wavelength of the surface waves. Then, to compute RS, we took u_3 and u_4 (similarly to u_1 and u_2) represented the de-meaned along-beam velocities V_3 and V_4 (see Eq. A1), respectively and were partitioned into turbulent and wave components. From the subtraction of the velocities u_3 and u_4 at $z^{(2)}$ and scaled it by an an attenuation parameter β obtained from the velocities at $z^{(1)}$, the application of VM gives an average value of the wave corrected RS component between positions 1 and 2 along beams 3 and 4:

$$-\overline{v'w'}^{(1-2)} \approx \frac{\overline{\Delta u_4^2} - \overline{\Delta u_3^2}}{4\sin\theta\cos\theta(1 + \beta^2)} \tag{B3}$$

where $\overline{\Delta u^2}$ denotes the difference of the de-meaned velocity variances. Note that the equation for $-\overline{u'w'}^{(1-2)}$ is inferred similarly.

Evaluation of the Reynolds stress using Eq. (B3) requires specification of the wave attenuation parameter, β. This is assumed to be time invariant and defined as:

$$\beta \approx \sqrt{\frac{\overline{(\tilde{u}^{1}_{\text{beam.fit}})^2}}{\overline{(\tilde{u}^{2}_{\text{beam.fit}})^2}}} \qquad\qquad (B4)$$

where $\overline{(\tilde{u}^{1,2}_{\text{beam.fit}})^2}$ are the variances at $z^{(1)}$ and $z^{(2)}$ due to the wave motion. The wave

5   variances were computed from linear wave theory using wave parameters determined

by fitting a model along-beam variance profile, $\overline{(\tilde{u}^{1,2}_{\text{beam}})^2}$, to the observed along-beam variance profile. For a beam axis aligned with the direction of wave propagation, the model variance profile is expressed by the following equation (Whipple et al., 2006):

$$\overline{(\tilde{u}_{\text{beam}})^2} = c_1[\cosh c_2(z + h) - \cos^2 \theta] \qquad\qquad (B5)$$

10   where $c_1 = H^2\omega^2/16\sinh^2 kh$, $c_2 = 2k$, H is wave height, ω is wave frequency, k is wavenumber and h is the total water depth. For a beam pair oriented at some angle α to the direction of wave propagation, the expression for beam velocity variance as a function of depth was found by Rosman et al. (2008):

$$\overline{(\tilde{u}_{\text{beam}})^2} = c_1[(\cos^2 \alpha \sin^2 \theta + \cos^2 \theta)\cosh c_2(z + h) + (\cos^2 \alpha \sin^2 \theta - \cos^2 \theta)] \qquad (B6)$$

15   Following Rosman et al. (2008), the beam velocity time series were segmented into intervals over which the flow is statistically stationary (Δt, here 10 min), and the means are removed from the beam velocities over these time intervals. Since according to our observation the direction of the wind wave propagation relative to the instrument, in period of storms, α, was about 15°, we used this angle in Eq. (B6). Beam velocity

20   variance, $\overline{(\tilde{u}_{\text{beam}})^2}$, was calculated over each interval, and the expression in Eq. (B6) was fit to each variance profile to obtain the parameters c_1 and c_2. To remove the wave

component of the beam velocity, two bins were selected at levels $z^{(1)}$ and $z^{(2)}$, centered on the height at which the Reynolds stress is required and spaced far enough apart that the turbulence is not correlated. We have chosen $\Delta z = 1.5\,\mathrm{m}$. The beam velocities at the two heights are differenced according to $\Delta u_{\mathrm{beam}} = u_{\mathrm{beam}}^{(1)} - \beta u_{\mathrm{beam}}^{(2)}$. Corrected

5   Reynolds stresses were estimated from Eq. (B3). Note that, as was analyzed by Rosman et al. (2007), VF method effectively removes wave-induced bias of RS, but there some limitation of this method associated with non-linearity of wind waves.

INSU
Institut national des **sciences** de **l'Univers**

The publication of this article is financed by CNRS-INSU.

15   ## References

Brylinski, J. M., Brunet, C., Bentley, D., Thoumelin, G., and Hilde, D.: Hydrography and phytoplankton biomass in the Eastern English Channel in spring 1992, Estuar. Coast. Shelf Sci., 43, 507–519, 1996.

Fredersen, F. and Williams III, A. J.: Direct estimation of the Reynolds stress vertical structure

20   in the nearshore, J. Atmos. Ocean. Tech., 24, 102–116, 2007.

Fugate, D. C. and Chant, R. J.: Near-bottom shear stresses in a small, highly stratified estuary, J. Geophys. Res., 110, C03022, doi:10.1029/2004JC002563, 2005.

Huang, Y. X., Schmitt, F. G., Lu, Z. M., Fougairolles, P., Gagne, Y., and Liu, Y. L.: Second order structure functions in fully developed turbulence, Phys. Rev. E, 82, 026319, doi:10.1103/PhysRevE.82.026319, 2010.

Kirincich, A. R., Lentz, S. J., and Gerbi, G. P.: Calculating Reynolds Stresses from ADCP measurements in the presence of surface gravity waves using the cospectra-fit method, J. Atmos. Ocean. Tech., 27, 889–907, 2010.

Korotenko, K. A. and Sentchev, A. V.: On the formation of anomalies in the ichthyoplankton concentration field along the French coast in the Eastern English Channel, Oceanology, 44, 644–653, 2004.

Korotenko, K. A. and Sentchev, A. V.: Effects of the particle migration on the features of their transport by tidal currents in the region of freshwater influence, Oceanology, 48, 672–684, 2008.

Korotenko, K. A. and Sentchev, A. V.: Study turbulence in shallow tidal coastal zone, Oceanology, 51, 1–14, 2011.

Lohrmann, A., Hackett, B., and Roed, L. P.: High resolution measurements of turbulence, velocity, and stress using a pulse-to-pulse coherent sonar, J. Atmos. Ocean. Tech., 7, 19–37, 1990.

Lu, Y. and Lueck, R. G.: Using a broadband ADCP in a tidal channel. Part I: mean flow and shear, J. Atmos. Ocean. Tech., 16, 1556–1567, 1999a.

Lu, Y. and Lueck, R. G.: Using a broadband ADCP in a tidal channel. Part II: mean flow and shear, J. Atmos. Ocean. Techn., 16, 1568–1579, 1999b.

Nidzieko, N. J., Fong, D. A., and Hench, J. L.: Comparison of Reynolds stress estimates derived from standard and fastping ADCPs, J. Atmos. Ocean. Tech., 23, 854–861, 2006.

Peters, H.: Observations of stratified turbulent mixing in an estuary. Neap-to-spring variations during high river run-off, Estuar. Coast. Shelf Sci., 45, 69–88, 1997.

Peters, H. and Johns, W. E.: Bottom layer turbulence in the Red Sea outflow plume, J. Phys. Oceanogr., 36, 1763–1785, 2006.

Peters, H., Lee, C. M., Orlic, M., and Dorman, C. E.: Turbulence in the wintertime Northern Adriatic Sea under strong atmospheric forcing, J. Geophys. Res., 112, C03S09, doi:10.1029/2006JC003634, 2007.

Plueddemann, A. J., Smith, J. A., Farmer, D. M., Weller, R. A., Crowford, W. R., Pinkel, R., Vagle, S., and Gnanadesikan, A.: Structure and variability of Langmuir Circulation during the Surface Waves Processes Program, J. Geophys. Res., 101, 3525–3543, 1996.

Effect of variable winds on current structure and Reynolds stresses

K. A. Korotenko et al.

Title Page

Abstract	Introduction
Conclusions	References
Tables	Figures

| ◄◄ | ►► |
| ◄ | ► |

Back | Close

Full Screen / Esc

Printer-friendly Version

Interactive Discussion

Discussion Paper | Discussion Paper | Discussion Paper | Discussion Paper

Rascle, N., Ardhuin, F., Queffeulou, P., and Croizé-Fillon, D.: A global wave parameter database for geophysical applications. Part 1: wave-current–turbulence interaction parameters for the open ocean based on traditional parameterizations, Ocean Model., 25, 154–171, 2008.

Rippeth, T. P., Williams, E., and Simpson, J. H.: Reynolds stress and turbulent energy production in a tidal channel, J. Phys. Oceanogr., 32, 1242–1251, 2002.

Rippeth, T. P., Simpson, J. H., Williams, E., and Inall, M. E.: Measurement of the rates of production and dissipation of turbulent kinetic energy in an energetic tidal flow: Red Wharf Bay revisited, J. Phys. Oceanogr., 33, 1889–1901, 2003.

Rosman. J. H., Hench, J. L., Koseff, J. R., and Monismith, S. G.: Extracting Reynolds stresses from acoustic Doppler current profiler measurements in wave dominated environments, J. Atmos. Ocean. Tech., 25, 286–306, 2008.

Schmitt, F. G., Huang, Y., Lu, Z., Liu, Y., and Fernandez, F.: Analysis of velocity fluctuations and their intermittency properties in the surf zone using empirical mode decomposition, J. Marine Syst., 77, 473–481, 2009.

Seim, H.: Reynolds stress measurements in a short tidal inlet, in: Proc. 2nd Meeting on the Physical Oceanography of Sea Straits, Villefranche, 15–19 April 2002, 199, 199–202, 2002.

Sentchev, A. and Korotenko, K. A.: Stratification and tidal current effects on larval transport in the Eastern English Channel: observations and 3D modelling, Environ. Fluid Mech., 4, 305–331, 2004.

Sentchev, A. and Korotenko, K. A.: Dispersion processes and transport patterns in the ROFI of Eastern English Channel derived from a particle tracking method, Cont. Shelf Res., 25, 2293–2308, 2005.

Sentchev, A. and Yaremchuk, M.: VHF radar observations of surface currents off the Northern Opal coast in the Eastern English Channel, Cont. Shelf Res., 27, 2449–2464, 2007.

Shaw, W. J. and Trowbridge, J. H.: The measurement of near-bottom turbulent fluxes in the presence of energetic wave motions, J. Atmos. Ocean. Tech., 18, 1540–1557, 2001.

Souza, A. J. and Howarth, M. J.: Estimates of Reynolds stress in a highly energetic shelf sea, Ocean Dynam., 55, 490–498, 2005.

Stacey, M. T., Monismith, S. G., and Burau, J. R.: Measurements of Reynolds stress profiles in unstratified tidal flow, J. Geophys. Res., 104, 10933–10949, 1999.

Tennekes, H. and Lumley, J. L.: A First Course in Turbulence, MIT Press, Cambrige, MA, 1972.

Discussion Paper | Discussion Paper | Discussion Paper | Discussion Paper | Discussion Paper

Terray, E. A., Donelan, M. A., Agarwal, Y. C., Drennan, W. M., Kahma, K. K., Williams III, A. J., Hwang, P. A., and Kitaigorodskii, S. A.: Estimate of kinetic energy dissipation under breaking waves, J. Phys. Oceanogr., 26, 792–807, 1996.

Trowbridge, J. H.: On a technique for measurement of turbulent shear stress in the presence of surface waves, J. Atmos. Ocean. Tech., 15, 290–298, 1998.

Trowbridge, J. H. and Elgar, S.: Spatial scales of stress-carrying nearshore turbulence, J. Phys. Oceanogr., 33, 1122–1128, 2003.

Wavenet: Wavenet archive, available online: www.cefas.co.uk/wavenet (last access: 12 June 2012), 2009.

Whipple, A. C., Luettich, R. A., and Seim, H. E.: Measurements of Reynolds stress in a wind-driven lagoonal estuary, Ocean Dynam., 56, 169–185, 2006.

Title Page

Abstract | Introduction

Conclusions | References

Tables | Figures

◄ | ►

◄ | ►

Back | Close

Full Screen / Esc

Printer-friendly Version

Interactive Discussion
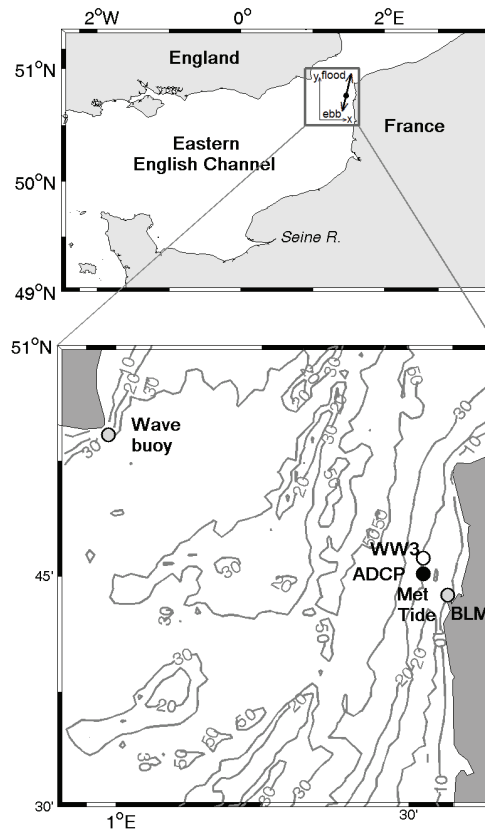
Fig. 1. The Eastern English Channel (upper panel) and location of the ADCP deployment site (black circle) in the Strait of Dover (lower panel). Grey circles denote location of the CEFAS wave buoy, Boulogne-sur-Mer lighthouse and tidal gauge (BLM). The open circle denotes the location of the grid point of the WW3 wave model closest to the ADCP location. The bottom topography is also shown. The x-y plane and direction of ebb and flood flows are shown in the upper panel.

Title Page

Abstract | Introduction

Conclusions | References

Tables | Figures

|◄ | ►|

◄ | ►

Back | Close

Full Screen / Esc

Printer-friendly Version

Interactive Discussion

Fig. 2. Time series of **(a)** wind stick diagram, **(b)** wind gusts (black) and averaged wind speed (gray) **(c)**, H_S observed by ADCP (gray) and CEFAS buoy (black thin), and predicted by WW3 (black thick), **(d)** wave (black) and wind (gray) directions. Two distinct storm events and calm periods, identified based on the wind speed and wave height records are annotated above the panel **(b)**. In the panel **(c)**, flood and ebb phases are indicated on SSH by 1 and 2, respectively. Flood periods are shaded.
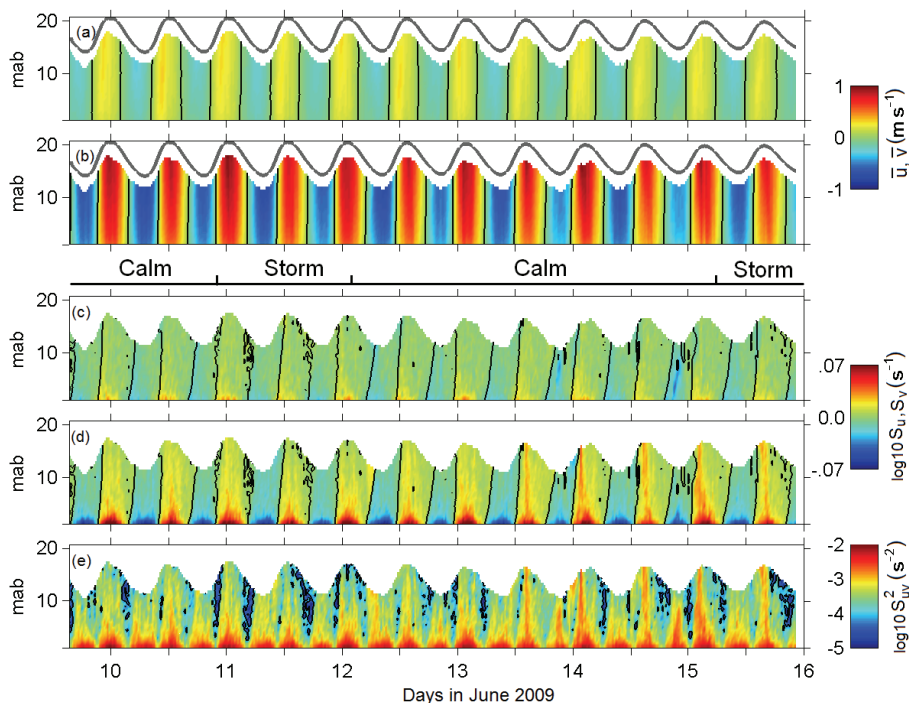
Fig. 3. Time-depth variability of **(a)** cross-shore mean current velocity $\overline{u}$ and **(c)** its shear $S_U = \mathrm{d}\overline{v}/\mathrm{d}z$, **(b)** along-shore mean current velocity, $\overline{v}$ and **(d)** its shear $S_V = \mathrm{d}\overline{v}/\mathrm{d}z$, and **(e)** shear velocity squared, S_{uv}^2. Sea level is marked by bold solid line over the velocity components. Zero-mean velocity and shear components are marked by solid lines. The abbreviation "mab" denotes meters above the bottom. The storm and calm periods correspond to those indicated in Fig. 2.
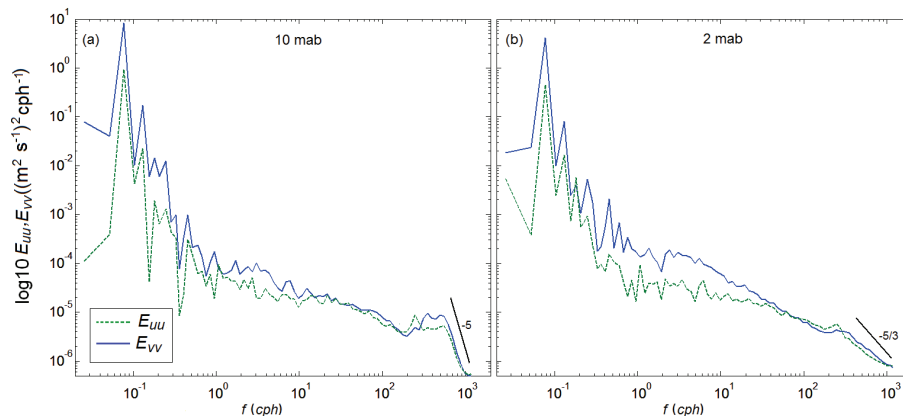
Fig. 4. Power spectral density for along-shore, E_{uu} (dashed) and cross-shore E_{vv} (solid) components of the horizontal velocity at **(a)** 10 and **(b)** 2 mab computed for the second calm period. Solid black lines represent the −5/3 slope expected for an inertial subrange.

Fig. 5. A sample of one day of along-shore velocity data collected at middepth (5 mab) in the period of **(a)** the storm on 11 June 2009 and **(b)** the calm on 13 June 2009.
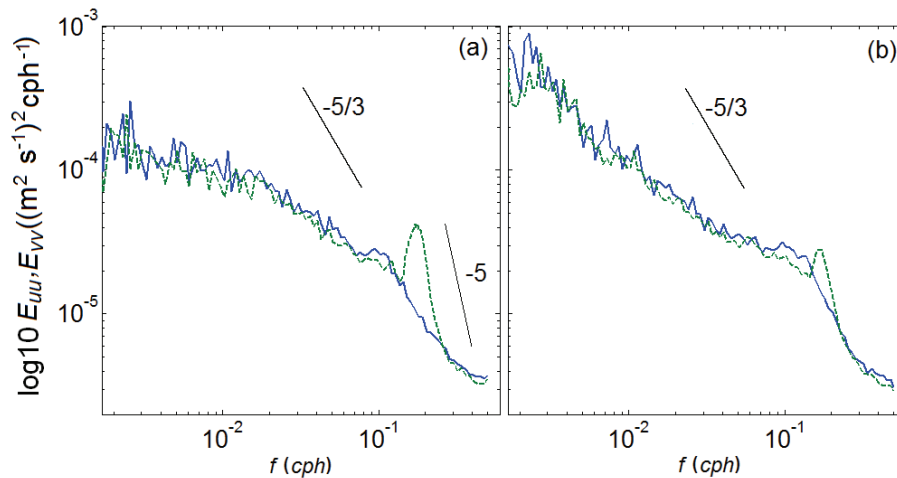
Fig. 6. Power spectral density of **(a)** cross-shore, E_{uu} and **(b)** along-shore, E_{vv} components of velocity at 4 mab for calm (solid) and storm (dashed) periods as in Fig. 5.
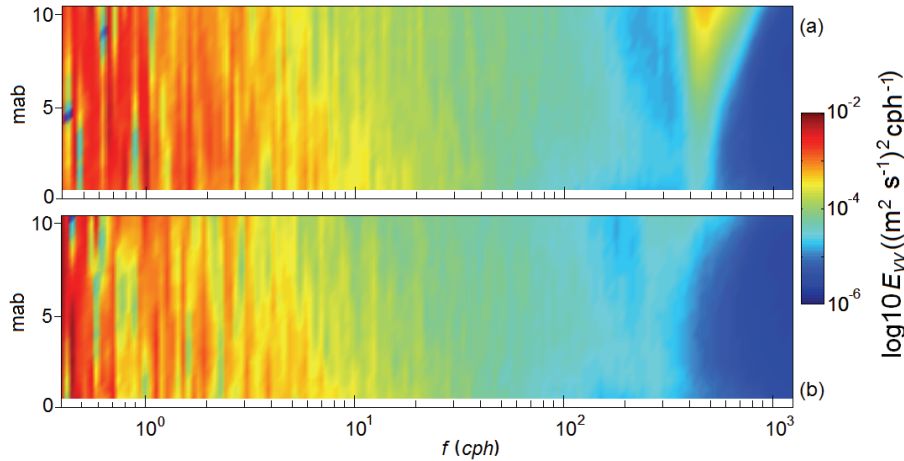
Fig. 7. 2-D-power spectral density of the along-shore current velocity for **(a)** storm and **(b)** calm periods, as shown in Fig. 5.
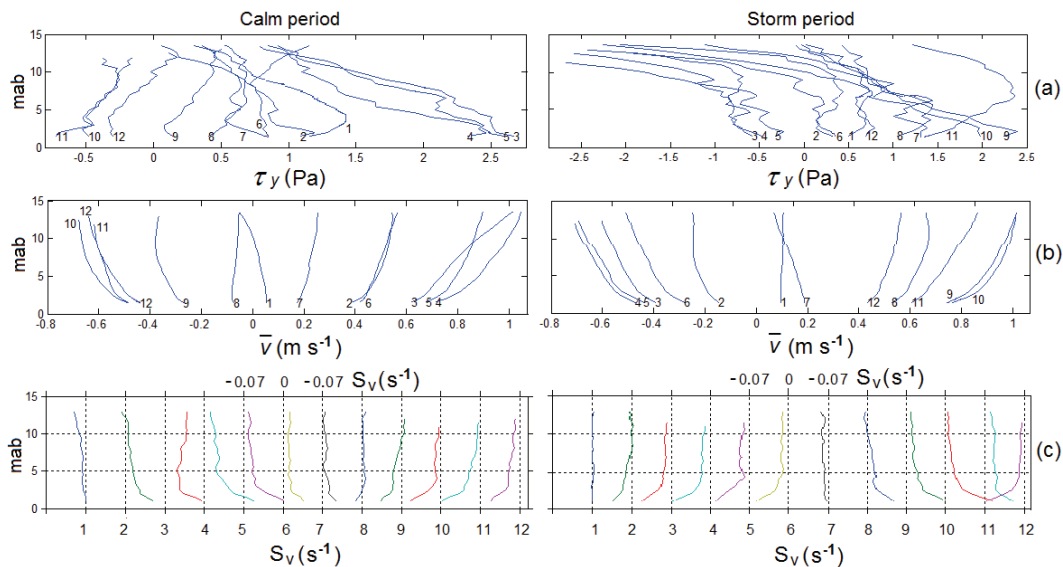
Fig. 8. Profiles of the along-shore mean velocity, $\overline{v}$, uncorrected Reynolds stress, τ_y, and shear, S_V over a single tidal cycle during the calm (left) and storm (right) periods. Numbers indicate the sequence of the hourly measurements/estimations. Reynolds stress profiles averaged over each hour of the tidal cycle. For the shear **(c)**, the scale is provided along the upper horizontal axis and ranges from $-0.07\,\mathrm{m\,s^{-1}}$ to $0.07\,\mathrm{m\,s^{-1}}$ for each individual profile. Vertical dashed lines correspond to a zero-crossing line for individual profiles.
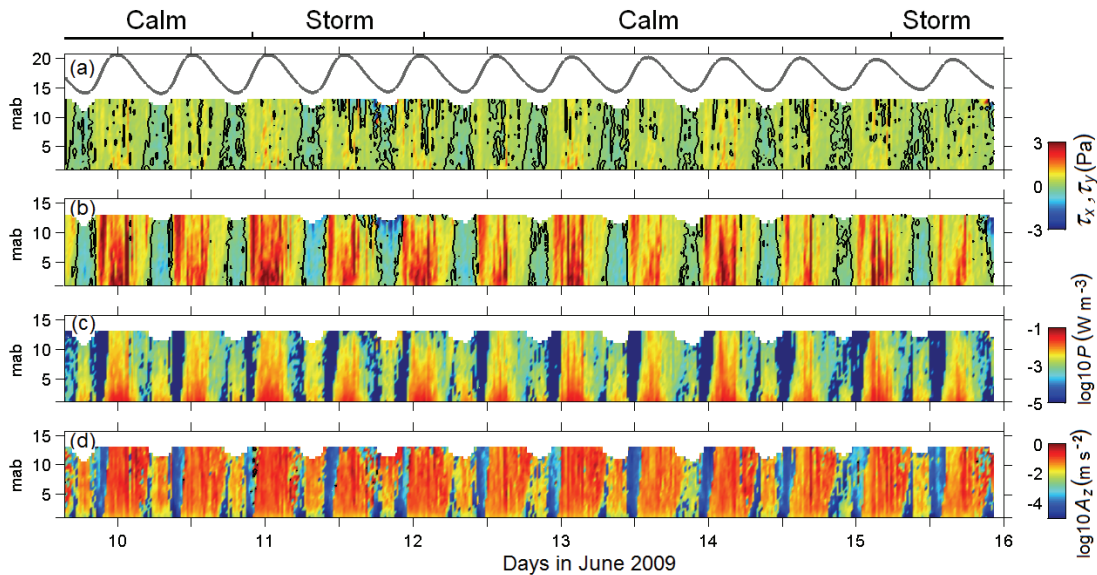
Fig. 9. Time-depth variations of (**a** and **b**) RS, **(c)** TKE production rate, P, and **(d)** turbulent viscosity, A_z corrected with VF method (Appendix B). The sea level **(a)** and zero-stress components (**a** and **b**) are marked by solid black lines.
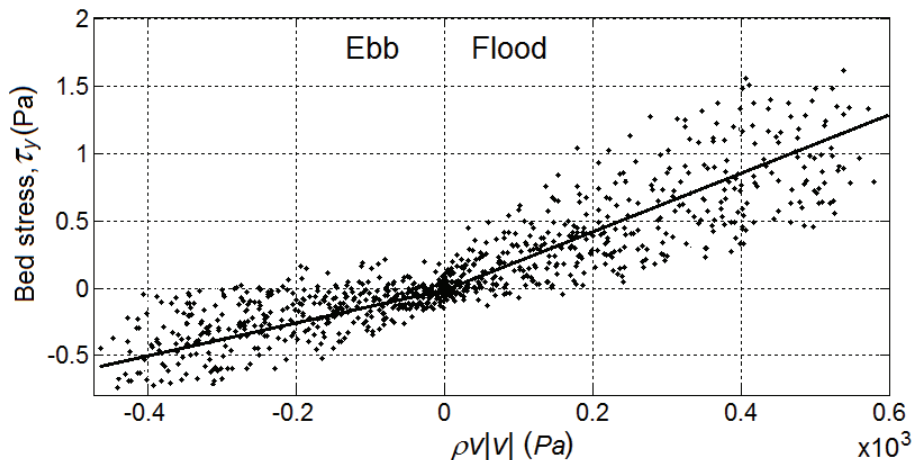
Fig. 10. Squared along-shore velocity at 2 mab and 10 min average the Reynolds stress averaged over 1.5–4.0 mab. Linear fits for the flood flow yielded a drag coefficient of 0.0022 and fits for the ebb flow yielded a drag coefficient of 0.0012.